

# Constraint of Non-thermal X-ray Emission from the On-going Merger Cluster Abell 3376 with Suzaku

Naomi KAWANO<sup>1</sup>, Yasushi FUKAZAWA<sup>1</sup>, Sho NISHINO<sup>1</sup>, Kazuhiro NAKAZAWA<sup>2</sup>,  
Takao KITAGUCHI<sup>2</sup>, Kazuo MAKISHIMA<sup>2,5</sup>, Tadayuki TAKAHASHI<sup>3</sup>,  
Motohide KOKUBUN<sup>3</sup>, Naomi OTA<sup>3</sup>, Takaya OHASHI<sup>4</sup>, Naoki ISOBE<sup>5</sup>,  
J. Patrick HENRY<sup>6</sup>, and Ann HORNSCHEMEIER<sup>7</sup>

<sup>1</sup>*Department of Physical Science, Hiroshima University, 1-3-1 Kagamiyama,  
Higashi-Hiroshima, Hiroshima 739-8526*

*kawano@hirax7.hepl.hiroshima-u.ac.jp, fukazawa@hirax7.hepl.hiroshima-u.ac.jp*

<sup>2</sup>*Department of Physics, University of Tokyo, 7-3-1 Hongo, Bunkyo, Tokyo 113-0033*

<sup>3</sup>*Department of High Energy Astrophysics, Institute of Space and  
Astronomical Science (ISAS), Japan Aerospace Exploration Agency (JAXA),  
3-1-1 Yoshinodai, Sagami-hara, Kanagawa 229-8510*

<sup>4</sup>*Department of Physics, Tokyo Metropolitan University,  
1-1 Minami-Osawa, Hachioji, Tokyo 192-0397*

<sup>5</sup>*Cosmic Radiation Laboratory, The Institute of Physical and Chemical Research (RIKEN),  
2-1 Hirosawa, Wako, Saitama 351-0198*

<sup>6</sup>*Institute for Astronomy, University of Hawai'i, 2680 Woodlawn Drive,  
Honolulu, HI 96822, USA*

<sup>7</sup>*Exploration of the Universe Division, NASA/Goddard Space Flight Center (GSFC),  
Greenbelt, MD, 20771, USA*

(Received 2007 0; accepted 2008 0)

## Abstract

Clusters of galaxies are among the best candidates for particle acceleration sources in the universe, a signature of which is non-thermal hard X-ray emission from the accelerated relativistic particles. We present early results on Suzaku observations of non-thermal emission from Abell 3376, which is a nearby on-going merger cluster. Suzaku observed the cluster twice, focusing on the cluster center containing the diffuse radio emission to the east, and cluster peripheral region to the west. For both observations, we detect no excess hard X-ray emission above the thermal cluster emission. An upper limit on the non-thermal X-ray flux of  $2.1 \times 10^{-11}$  erg cm<sup>-2</sup> s<sup>-1</sup> (15–50 keV) at the  $3\sigma$  level from a  $34 \times 34$  arcmin<sup>2</sup> region, derived with the Hard X-ray Detector (HXD), is similar to that obtained with the BeppoSAX/PDS. Using the X-ray Imaging Spectrometer (XIS) data, the upper limit on the non-thermal emission

from the West Relic is independently constrained to be  $< 1.1 \times 10^{-12}$  erg s<sup>-1</sup> cm<sup>-2</sup> (4–8 keV) at the  $3\sigma$  level from a 122 arcmin<sup>2</sup> region. Assuming Compton scattering between relativistic particles and the cosmic microwave background (CMB) photons, the intracluster magnetic field  $B$  is limited to be  $>0.03\mu\text{G}$  (HXD) and  $>0.10\mu\text{G}$  (XIS).

**Key words:** galaxies: clusters: individual (Abell 3376) – X-rays: galaxies – X-rays: non-thermal emission

## 1. Introduction

Particle acceleration is one of the most exciting phenomena in clusters of galaxies. In fact, Mpc-scale diffuse synchrotron emission has been reported for many clusters of galaxies (e.g. Giovannini et al. 1993), implying that the relativistic electrons surely exist. A natural origin of acceleration in clusters is merger shocks. The electrons, accelerated to relativistic speeds by a strong cluster merger (e.g. Takizawa & Naito 2000; Fujita & Sarazin 2001), scatter off the cosmic microwave background (CMB) photons via the inverse Compton process. This causes non-thermal hard X-ray emission which may exceed the thermal bremsstrahlung emission of the intracluster medium (ICM) at energies above several tens of keV. Studies of inverse Compton emission in addition to the radio synchrotron are important to measure the energy densities of the magnetic field and electrons without assuming equipartition. Since the cooling time of such high energy electrons is relatively short,  $\sim 10^8$  yr, they vanish rapidly during cluster evolution. Another mechanism to produce a nonthermal electron population is via proton-proton collisions between the relativistic protons and the ICM protons. In this case, the relativistic electrons can be provided for a long time because the lifetime of relativistic protons is comparable to that of galaxy cluster ( $\sim H_0^{-1}$ ). Such protons may also cause a gamma-ray emission through  $\pi^0$  decays. Contribution of non-thermal pressure to the thermal one is also an important question, since it could affect the cluster mass estimation under the assumption of hydrostatic equilibrium. Accordingly, hard X-ray and gamma-ray measurements of non-thermal cluster emission are important issues and so far many attempts have been performed. Furthermore, the launch of the GLAST satellite scheduled in 2008 will improve the GeV gamma-ray survey in the near future.

Some detections of non-thermal hard X-rays of varying levels of significance have been reported by the BeppoSAX/PDS, ASCA/GIS, and RXTE/PCA. Individual detections have been reported of the Coma cluster (Fusco-Femiano et al. 1999), Abell 2256 (Fusco-Femiano et al. 2000), Abell 2199 (Kaastra et al. 1999), Abell 3667 (Fusco-Femiano et al. 2001), and HCG 62 (Fukazawa et al. 2001, Nakazawa et al. 2007). From the systematic analysis of 27 clusters using BeppoSAX PDS data, a possible excess signal of non-thermal emission was reported for 7 galaxy clusters with  $>2\sigma$  level (Nevalainen et al. 2004). The reported hard X-ray luminosity of these clusters is in a range of  $(0.17-42)\times 10^{43}$  erg s<sup>-1</sup>, which corresponds

to 1–20 % of the thermal luminosity. The spatial distribution is as important to understand the non-thermal view of galaxy clusters as is spectral information. However, the spatial extent of the non-thermal hard X-ray emission has not been measured yet.

Abell 3376 (DC 0559-40) is a nearby ( $z=0.046$ ), rich cluster of galaxy. A binary sub-cluster merger is occurring in this cluster, and a weak positive hard X-ray signal ( $2.7\sigma$ ) with the BeppoSAX/PDS was reported by Nevalainen et al. (2004). Another remarkable feature of this cluster is a pair of Mpc scale radio relics (Bagchi et al. 2005; Bagchi et al. 2006). The 1.4 GHz radio flux densities of two relics from the VLA NVSS are  $32\pm 3$  mJy and  $82\pm 5$  mJy for the east (ER) and the west relic (WR), respectively. Radio relics are considered to be synchrotron emission generated through the interaction between electrons accelerated by merger shock and magnetic field in the ICM, implying that the relativistic electrons really exist in this cluster. The giant ringlike structure of the radio relics imply a strong shock wave which could accelerate particles up to  $10^{18-19}$  eV (Bagchi et al. 2006). The thermal properties of this cluster have been observed with ROSAT, ASCA, Chandra, and XMM-Newton. The ICM temperature reported by XMM-newton (Bagchi et al. 2006) is moderately low ( $\sim 4$  keV), similar to that of the ASCA observation (Fukazawa et al. 2004), and we can therefore search for the non-thermal emission by avoiding thermal component in the energy band above 10 keV. From these properties, Abell 3376 emerged as a good candidate to search for the non-thermal hard X-ray emission. In this paper, we present early results of Suzaku observation of Abell 3376, focusing on the non-thermal hard X-ray emission.

The Si-PIN diode (PIN) in the Hard X-ray detector (HXD; Takahashi et al. 2007; Kokubun et al. 2007) onboard Suzaku has a very low background in the 10–30 keV band; the background count rate normalized by the effective area is smaller than any past instrument. In addition, its narrow field of view ( $34'\times 34'$  full width at half maximum, FWHM), compared with the BeppoSAX/PDS ( $1.3^\circ$  hexagonal FWHM) and RXTE/PCA ( $1^\circ$  hexagonal FWHM), yields several advantages. First, the confusion from hard point sources is reduced, as is the contribution of the ICM thermal emission, and finally the non-thermal emission may be localized better. Suzaku also employs the X-ray Imaging Spectrometer (XIS; Koyama et al. 2007), which consists of one back-illuminated (BI) CCD chip (XIS1), and three front-illuminated (FI) CCD chips (XIS0, 2, 3). Since the XIS also achieves the lowest background level of any previous X-ray CCD, it is useful to constrain the hard X-ray emission.

Throughout this paper, we adopt a Hubble constant of  $H_0=50 h_{50}$  km s $^{-1}$  Mpc $^{-1}$ , which implies that  $1'$  corresponds to 80.3 kpc in the cluster frame. All statistical errors are given at the 90 % confidence level unless otherwise indicated.

## 2. Observations and Data Reduction

Two long observations of Abell 3376 were carried out on October 6–10 and November 7–10, 2005, in Suzaku Phase-I period (i.e. initial performance verification period). The former

observation included the cD galaxy and the ER. The latter one focused on the WR, which is  $\sim 25'$  west of the cD galaxy. The details of each observation are shown in Table 1. Both the XIS and HXD were operated in the normal mode. Figure 1 shows an X-ray image of Abell 3376 obtained with the XIS in the 0.5–8.0 keV band. The thermal emission has an X-ray peak around the cD galaxy and is elongated due to the subcluster merging as observed with previous satellites (Bagchi et al. 2005; Bagchi et al. 2006).

We used version 1.2 pipeline processing data (Mitsuda et al. 2007), and the data reduction was performed with `HEASOFT` version 6.2. For the HXD data, events are filtered with a cut-off rigidity (COR) of  $> 6 \text{ GeV c}^{-1}$ , elevation angle of  $> 5^\circ$  from the earth rim, and good time interval (GTI) during which the satellite is outside the South Atlantic Anomaly (SAA). Moreover, we eliminate the periods ( $\sim 500 \text{ s}$ ) when the PIN count rate is flaring due to in-orbit particles. After these procedures, a net PIN exposure time of 90 ks and 103 ks was obtained for the Center/ER and WR pointing, respectively. We applied `ae_hxd_pinhxnom_20060419.rmf` for the HXD response matrix. The PIN detector background is estimated by our own method rather than the standard model, as described in §3.1. We do not present the GSO data in this paper, since no significant signal is detected.

Selection criteria are different for the XIS compared to the HXD only in the respect that the earth elevation angle of  $> 20^\circ$  is applied. We also examined the 0.5–8 keV light curve with 128 s time bin to remove the flaring periods of the event rate higher than  $\pm 3\sigma$  above the average. The resulting exposure times become 120 ks and 127 ks for the Center/ER and WR observations, respectively. We generated the response matrix files with the `xisrmfgen` FTOOLS task, and the auxiliary response files with the `xissimarfgen` FTOOLS task (Ishisaki et al. 2007). The latter takes into account the vignetting effect and corrects the efficiency degradation in the lower energy band due to contamination on the optical blocking filters in front of the XIS (Koyama et al. 2007). The ROSAT PSPC image of Abell 3376 was used as the seed image in the `xissimarfgen`, and also the regions of extracted spectra are taken into account. The detector background is estimated by the FTOOLS task `xisntebgdgen` (Tawa et al. 2007). We performed spectral fits in the energy range of 0.3–8.0 keV and 0.5–8.0 keV for the XIS BI and the FI, respectively. The energy range of 1.7–1.9 keV is ignored in the spectral fitting of XIS because the response matrix around Si-K edge has some residual uncertainties. All the spectral analyses were performed with XSPEC 11.2.0.

**Table 1.** Suzaku observation log of Abell 3376

Position	Sequence No.	Date	RA, DEC	Exposure time*
Center/East Relic	100034010	2005 Oct. 6–10	06 <sup>h</sup> 02 <sup>m</sup> 15.0 <sup>s</sup> , -39°57′00.0″	90 ks / 120 ks
West Relic	800011010	2005 Nov. 7–10	06 <sup>h</sup> 00 <sup>m</sup> 00.0 <sup>s</sup> , -40°01′58.8″	103 ks / 127 ks

\*: The net exposure time of HXD/XIS after the events are screened.

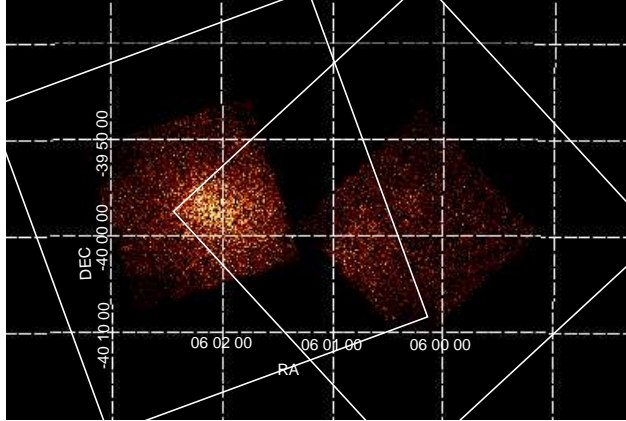


**Fig. 1.** Suzaku XIS image of Abell 3376 in the 0.5–8 keV band. All the BI and FI data from the two pointings are combined. The corner regions illuminated by the calibration source are excluded. The large squares represent the HXD-PIN field of view with a FWHM of  $34' \times 34'$ .

### 3. Data Analysis and Results

#### 3.1. Spectral Analysis

##### 3.1.1. HXD Spectra

First, we explore the non-thermal emission with the HXD PIN spectrum. Five components are here considered; ICM thermal emission, cosmic X-ray background (CXB), non-X-ray detector background (NXB), point sources, and possible non-thermal emission. Among these components, NXB contribution to the total counts is the highest. Therefore, it is most important to predict the NXB as accurately as possible for detection of faint non-thermal emission. The HXD team has officially supplied the NXB model for the PIN, which reproduces the NXB by sorting the earth-occultation data-base with two parameters; PINUD count and PINUD build-up count. The latter is a convolution of PINUD with an exponential function with an appropriate decay constant, in order to represent the activation-induced gamma-rays due to the SAA passage. Since this component is non-negligible for a day or so after the SAA passage, the PINUD count history just before the observation is needed to model the background of that observation. Unfortunately, the satellite telemetry data was not received for almost a day before the observation of A3376 WR (Nov 7–10, 2005), consequently the PINUD data are not available for that time period. Thus, the official NXB background model is not accurate, and here we apply an alternative background estimation. Our estimation method is based on the NXB count rate map sorted by latitude and longitude on the earth for the satellite position. We used earth occultation data as the NXB template. After the long-term variation is corrected, the NXB uncertainty finally becomes  $\sim 2\%$  at the  $1\sigma$  level, which is a similar reproducibility to that of the official NXB model. The details of our NXB estimation method and its systematic

uncertainty are described in Appendix 1.1. Further details are given in Kawano (2006). As a result, our NXB is consistent with the official NXB within their systematic errors even for the WR observation.

We examine the possible non-thermal emission by estimating the contribution of the other components to the NXB-subtracted spectra as follows. First for the ICM flux we used that within 19 arcmin measured by the ASCA/GIS,  $2.5 \times 10^{-11}$  erg cm<sup>-2</sup> s<sup>-1</sup> (0.5–10 keV) (Fukazawa et al. 2004). Since XIS detected the emission up to 22 arcmin, we extrapolated the above flux to 22 arcmin with a  $\beta$ -model with parameters obtained from the same ASCA/GIS data, yielding  $3.0 \times 10^{-11}$  erg cm<sup>-2</sup> s<sup>-1</sup> (0.5–10 keV). We used this value to normalize the X-ray surface brightness from an archival ROSAT/PSPC image, then folded the result through the PIN collimator transmission. The result is the total ICM flux that would be observed by the PIN if it were sensitive in the 0.5–10 keV band:  $2.1 \times 10^{-11}$  erg cm<sup>-2</sup> s<sup>-1</sup> and  $1.5 \times 10^{-11}$  erg cm<sup>-2</sup> s<sup>-1</sup> for the Center/ER and WR observation, respectively. We extrapolated the spectrum into the PIN energy band assuming the spectral parameters in Fukazawa et al. (2004), obtaining  $2.5 \times 10^{-13}$  erg cm<sup>-2</sup> s<sup>-1</sup> and  $1.8 \times 10^{-13}$  erg cm<sup>-2</sup> s<sup>-1</sup> (15–50 keV) for the Center/ER and WR observation, respectively. In order to check the consistency between PSPC/GIS and XIS, we estimated the XIS flux for both Center/ER and WR observations with `xissimarfgen` by using the same normalized PSPC image and assumed spectrum, confirming that the XIS flux and the estimated one are consistent within 10%.

Second, we estimated the flux and spectral shape of the CXB from the observational results of Kirsch et al. (2005). Specifically, we model the CXB spectrum by a powerlaw with a photon index of 1.4 with a cut-off at 40 keV. The surface brightness is again folded through the HXD field of view, yielding  $6.9 \times 10^{-12}$  erg s<sup>-1</sup> cm<sup>-2</sup> in 15–50 keV.

Third, we used the ROSAT 2RXP catalogue<sup>1</sup> order to model the contribution of point sources. This catalogue allows us to search for point sources over the whole HXD field of view. We found 2 (4) sources in the HXD-PIN field of the Center/ER (WR) observation. Assuming a powerlaw spectrum with photon index of 1.5 and the 2RXP normalization, the total point source contribution to each pointing is quite small,  $5.8$  ( $8.2$ )  $\times 10^{-13}$  erg s<sup>-1</sup> cm<sup>-2</sup> (15–50 keV) for the Center/ER (WR) region. The flux from obscured AGNs not detected by ROSAT is likely to also be small, as discussed in Nevalainen et al. (2004). Since the current PIN response gives a factor of 1.13 larger model normalization than the XIS response (Kokubun et al. 2007), we multiplied the flux of all the above components by this factor.

Figure 2 shows the NXB-subtracted spectra of the HXD PIN, together with each model component. We find a weak hard X-ray excess above 15 keV for Abell 3376 WR. When we assumed the excess emission to be a power-law with a photon index of 2.0, its flux is  $(7.2 \pm 2.4) \times 10^{-12}$  erg s<sup>-1</sup> cm<sup>-2</sup> (15–50 keV) at the 90% confidence level after the flux of the other components are excluded.

---

<sup>1</sup> <ftp://ftp.xray.mpe.mpg.de/rosat/catalogues/2rxp/pub>

We estimated the systematic uncertainty of each spectral component in order to determine whether the excess is significant. Fluxes are reported in the 15–50 keV range hereafter. The PIN NXB has a systematic uncertainty of 2 % at the  $1\sigma$  level as mentioned above. This gives the largest uncertainty, which corresponds to  $\sim 2.8 \times 10^{-12}$  erg s $^{-1}$  cm $^{-2}$ . For the ICM emission, the uncertainty of the flux (i.e. *normalization*) comes from modeling the surface brightness profile and assumption of the uniform temperature distribution. However, the ICM emission is much softer and fainter than the excess hard X-ray emission, and thus the ICM flux uncertainty cannot explain the excess emission. The systematic uncertainty of the CXB ( $\sigma_{\text{CXB}}$ ) arises from two reasons; an intrinsic intensity fluctuation on the sky (Kushino et al. 2002) and a systematic uncertainty of the normalization in past measurements. The fluctuation is calculated by scaling the HEAO-1 result of 2.8 % with the equation  $\sigma_{\text{CXB}} \propto \Omega^{-0.5} S^{0.25}$  (Condon 1974), where  $\Omega = 15.8$  deg $^2$  and  $S \sim 8 \times 10^{-11}$  ergcm $^{-2}$ s $^{-1}$  are the effective solid angle of the observation and upper cut-off flux of the detectable discrete sources in the field of view, respectively. In the case of the HXD ( $\Omega = 34' \times 34'$ , and  $S \sim 8 \times 10^{-12}$  ergcm $^{-2}$ s $^{-1}$ ), the systematic fluctuation of the CXB is calculated to be 9.2% ( $1\sigma$ ) of CXB flux. The normalization uncertainty is around 10% when we survey past measurements (Kirsch et al. 2005), corresponding to  $\sim 0.8 \times 10^{-12}$  erg s $^{-1}$  cm $^{-2}$ . Finally, for point sources, we consider the sum of the statistical errors of each point source obtained from ROSAT 2RXP catalogue as the systematic uncertainty. This gives a fluctuation of at most  $\sim 0.04 \times 10^{-12}$  erg s $^{-1}$  cm $^{-2}$  ( $1\sigma$ ). In summary, the dominant error source is the uncertainty of the PIN NXB estimation. We combined these systematic errors by summing squares.

Considering all the systematic uncertainties, the hard X-ray flux of A3376 WR is  $(7.2 \pm 4.8 \pm 8.8) \times 10^{-12}$  erg s $^{-1}$  cm $^{-2}$  at the  $3\sigma$  confidence level, where a photon index of 2.0 is assumed. Therefore, the non-thermal X-ray emission is not significant. The  $3\sigma$  upper limit is  $2.1 \times 10^{-11}$  erg s $^{-1}$  cm $^{-2}$ , by adding both the statistical and systematic errors at that level. In the same manner, the hard X-ray flux of A3376 ER is  $(3.2 \pm 2.4 \pm 8.8) \times 10^{-12}$  erg s $^{-1}$  cm $^{-2}$  at the  $3\sigma$  confidence level, and the  $3\sigma$  upper-limit flux for the Center/ER observation is derived to be  $1.4 \times 10^{-11}$  erg s $^{-1}$  cm $^{-2}$ ; . The flux detected with BeppoSAX/PDS is  $(8.0 \pm 8.9) \times 10^{-12}$  ( $3\sigma$  error) when scaled to the energy band of 15–50 keV by a power-law model with a photon index of 2.0 (Nevalainen et al. 2004), and thus the upper limit is similar to our results. Note that our constraint per unit solid angle,  $1.8 \times 10^{-14}$  erg cm $^{-2}$  s $^{-1}$  arcmin $^{-2}$ , is for a smaller sky region of  $34' \times 34'$  around the WR, while the BeppoSAX upper limit per unit solid angle,  $2.8 \times 10^{-15}$  erg cm $^{-2}$  s $^{-1}$  arcmin $^{-2}$ , is for a larger sky region of  $78' \times 78'$ .

### 3.1.2. *XIS Spectra*

The highest energy channels of the XIS are useful for searching for non-thermal emission in the periphery of clusters of galaxies since the XIS achieves the lowest NXB among the existing CCD detectors. We here present the results from the XIS spectral analysis. We first created the XIS NXB spectra by means of the background generator `xisntebgdgen`, in which the NXB

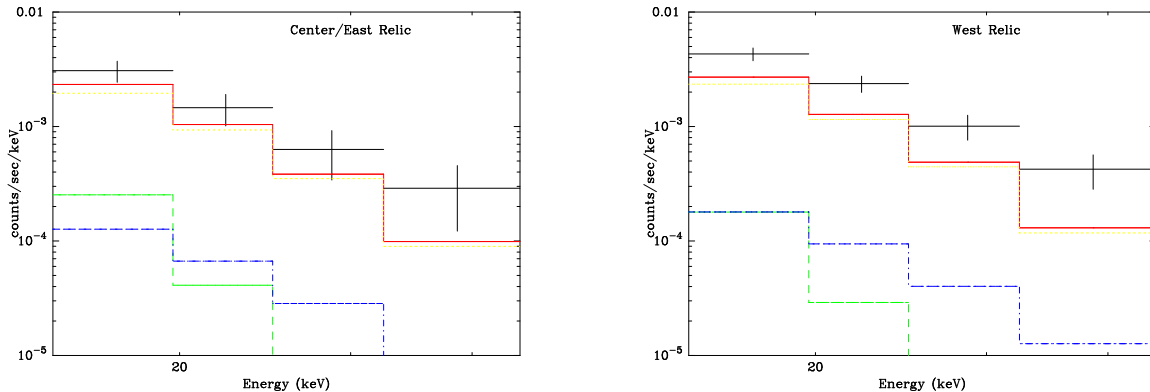


**Fig. 2.** NXB-subtracted HXD PIN spectra from Abell 3376 Center/ER (left) and WR (right). The black crosses show NXB-subtracted data while the solid lines correspond to the contribution of CXB (yellow), thermal ICM (green), point sources (blue), and their sum (red), respectively.

spectrum for the same detector region as the on-source spectra is estimated from the night earth observation database, based on the history of the COR in each observation. The reproducibility of the XIS NXB seems to be somewhat different among the four sensors (XIS0–3), and it is reported to be 2.8–4.4 % ( $1\sigma$ ) in the 5–12 keV band (Tawa et al. 2007).

The CXB spectrum is modeled by a power-law with a photon index of 1.4. We utilized the spectrum of the west region of WR, where the cluster emission is negligible, to measure the CXB normalization. We generated the auxiliary response files with `xissimarfgen`, assuming that the incident emission is spatially uniform and comes from a circle with 20 arcmin radius, combined with the integration region on the detector for the above spectrum. The spectrum at the west region of WR is completely consistent with the model in the high energy band, but additional low-temperature thermal emission, which is due to the Galactic emission, is needed in the lower energy band. We fitted these components by adding a two-temperature APEC plasma model of solar abundance, obtaining temperatures of 0.08 keV and 0.28 keV and the normalization for both. Then, we modeled the emission for the on-source region of the A3376 integration by preparing the auxiliary response file for that region and folding the above CXB and Galactic emission model through the XIS. We subtracted the thus-obtained background spectra and the NXB spectrum from the on-source spectra.

Figure 3 shows the hard band image in the 4–8 keV band for both Abell 3376 Center/ER and WR. A blank-sky image, extracted from the Lockman Hole observed on May 7, 2006, is subtracted as the background data from Abell 3376 source image. The 1.4 GHz radio contours are superposed. The cluster in the hard band exhibits an elongated appearance similar to that in the total band (Figure 1) or low energy band image, and there is no remarkable feature associated with the radio emission. The spectra of Abell 3376 are extracted from the full field of view of the XIS after excluding the calibration source region for the Center/ER observation, and from a hexagon region with a width of 6' covering the radio relic for the WR observation



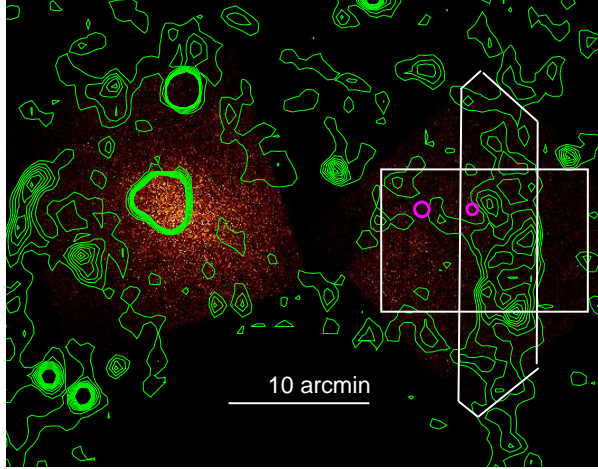


**Fig. 3.** Suzaku XIS image of Abell 3376 in the 4–8 keV band. All the images of XIS0–3 are merged. The 1.4 GHz radio contours of NVSS are superposed. Two magenta circles indicate the positions of point sources in the XIS field of view. The square represents the region of projection analysis. The hexagon represents the integration region for spectral analysis of the West Relic.

(Figure 3). Using the ROSAT PSPC image, we estimated the stray light from the bright cluster center to the WR region with `xissimarfgen`, and found that it is only 25%. The stray light contribution itself is already included in the `arf` files and the center and the WR spectra are similar. Before constraining the nonthermal emission, we first fitted the Abell 3376 spectra with a single temperature APEC plasma model, without an extra power-law component. The summary of the spectral fitting is shown in table 2 and figure 4. The ICM temperature and metal abundance of the Center/ER region are roughly consistent with the ASCA and XMM-Newton results (Fukazawa et al. 2004, Bagchi et al. 2005). On the other hand, the temperature in the WR region is somewhat lower. Next we included a power-law model to represent the nonthermal emission. The photon index is assumed to be 2.0 in the same manner as in the PIN analysis. The power-law component is significantly required for the Center/ER spectra, considering only the statistical error.

We consider the  $3\sigma$  systematic error arising from the uncertainties of the response matrix, background model, and ICM emission model, since the CXB fluctuations are at most 6% ( $3\sigma$ ) of the total flux. The first is  $0.6 (0.05) \times 10^{-12} \text{ erg s}^{-1} \text{ cm}^{-2}$  for the Center/ER (WR), by assigning a 10% error to the response matrix (Serlemitsos et al. 2007) and taking 10% of the observed total flux. For the second, we took a systematic uncertainty of the XIS NXB as 10 % at the  $3\sigma$  level, fitted the spectra by renormalizing the background by 0.9 and 1.1, and obtained the error from the allowed power-law flux range;  $0.2 \times 10^{-12} \text{ erg s}^{-1} \text{ cm}^{-2}$  for both the center/ER and WR observation. The residual around 7 keV in the Center/ER spectra almost disappears when the NXB level is raised by 5%. We estimate the error on the third by adding another APEC component to the model, since this cluster is merging and possibly consists of a

multi-temperature structure. For the center/ER spectra, this operation significantly improves the fit and the residual in the higher energy band almost disappears; the systematic error is  $2.0 (0.29) \times 10^{-12} \text{ erg s}^{-1} \text{ cm}^{-2}$  for the Center/ER (WR).

Taking into account the above systematic uncertainties, the flux of the power-law component is constrained to be  $(1.1 \pm 0.4 \pm 2.0) \times 10^{-12} \text{ erg s}^{-1} \text{ cm}^{-2}$  and  $(4.6 \pm 4.0 \pm 2.9) \times 10^{-13} \text{ erg s}^{-1} \text{ cm}^{-2}$  (4–8 keV) for the center/ER and WR, respectively, at  $3\sigma$  level. The detection of both observations is not significant, and therefore we obtain a  $3\sigma$  upper limit on the power-law flux in the 4–8 keV band:  $<3.5 \times 10^{-12} \text{ erg s}^{-1} \text{ cm}^{-2}$  (Center/ER), and  $<1.1 \times 10^{-12} \text{ erg s}^{-1} \text{ cm}^{-2}$  (WR). When they are extrapolated to the PIN energy band, the upper limit in the 15–50 keV band is  $<6.1 \times 10^{-12} \text{ erg s}^{-1} \text{ cm}^{-2}$  (Center/ER), and  $<1.9 \times 10^{-12} \text{ erg s}^{-1} \text{ cm}^{-2}$  (WR). This constraint gives a surface brightness per unit solid angle of  $<1.9 \times 10^{-14} \text{ erg s}^{-1} \text{ cm}^{-2} \text{ arcmin}^{-2}$  (Center/ER), and  $<1.5 \times 10^{-14} \text{ erg s}^{-1} \text{ cm}^{-2} \text{ arcmin}^{-2}$  (WR), similar to that of the upper limit of HXD-PIN for the WR,  $1.6 \times 10^{-14} \text{ erg s}^{-1} \text{ cm}^{-2}$ , when considering the difference of the field of view.

Since the Fe-K line may be affected by the non-thermal component, we fitted the XIS spectrum only around the Fe-K band (6–7 keV) with a single-temperature plasma model. The WR spectrum is too poor to perform such an analysis, and thus we here analyzed only the center/ER spectrum. We see a weak signature of the H-like Fe-K $\alpha$  line. However, the obtained temperature of  $4.6 \pm 0.5 \text{ keV}$  is consistent with the value of the whole-band spectral fitting. No significant deviation of the line ratio between He-like and H-like lines is observed. The upper limit of the Fe-K line broadening is  $1200 \text{ km s}^{-1}$ .

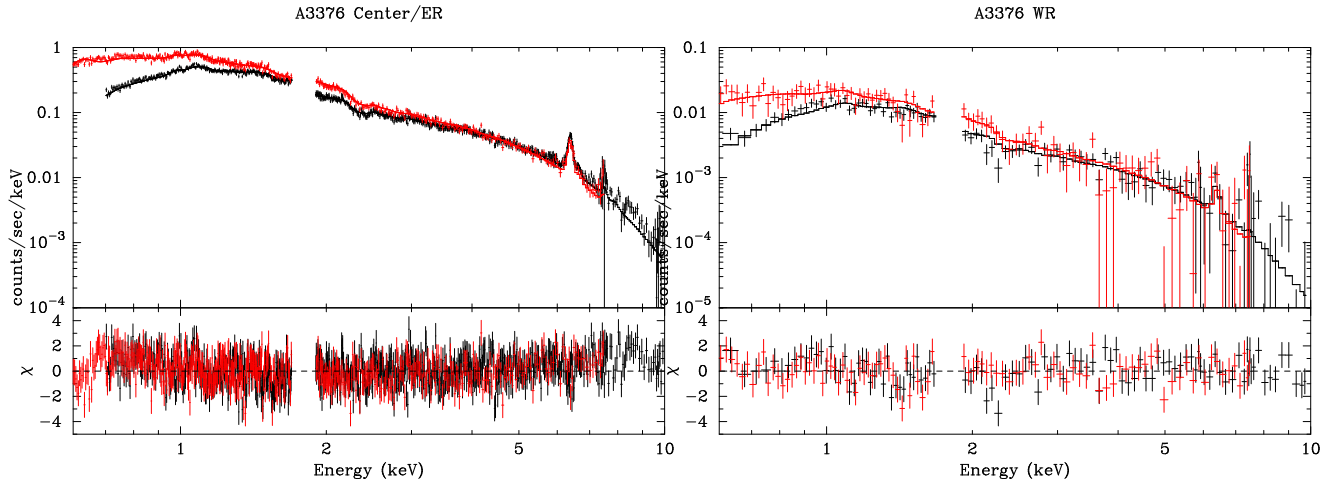


**Fig. 4.** Spectral fitting of XIS spectra from Abell 3376 Center/ER (left) and WR (right), with the thermal plasma model. The red and black represent the XIS-BI and FI, respectively. The crosses show background-subtracted data. The solid lines represent the best-fit model.

**Table 2.** Best-fit parameters for the XIS spectral fitting

Position	Temperature*	Abundance*	Reduced $\chi^2$ *	Reduced $\chi^2$ ‡	$F_{\text{po}}^\dagger$
Area	(keV)	(solar)	( $\chi^2/\text{d.o.f.}$ )	( $\chi^2/\text{d.o.f.}$ )	( $\text{erg s}^{-1} \text{ cm}^{-2}$ )
Center/East relic					
18 × 18 arcmin <sup>2</sup>	4.12±0.05	0.29±0.01	1.32 (1581/1201)	1.07 (1281/1200)	(1.1 ± 0.2)×10 <sup>-12</sup>
West Relic					
122 arcmin <sup>2</sup>	3.81±0.33	0.22±0.10	1.08 (171/158)	1.00 (157/157)	(4.6 ± 2.0)×10 <sup>-13</sup>

\* : Results for the model that does not contain the nonthermal power-law component.

‡ : Reduced  $\chi^2$  for the model that contains the nonthermal power-law component.

† : Allowed flux of the power-law component in 4–8 keV, when it is included in the spectral fitting.

Here only the statistical error is shown.

### 3.2. Comparison of X-ray and Radio Image around the West Relic

In order to compare the X-ray and radio image quantitatively, we extracted the count rate profiles along the east-west direction from the white square region in figure 3, and show the profiles in figure 5 along with the 1.4 GHz radio profile. The X-ray profile is divided into three energy bands; 1–2, 2–4, and 4–8 keV. The count rate is arbitrarily scaled so as to distinguish the difference among profiles easily. Two magenta circles in figure 3 show the positions of two point sources in the field of view. These are at pixels 1750 and 1970 in the profiles, and correspond to local enhancements in the projected count rate. The X-ray emission exhibits similar profiles among the three energy bands. The count rate ratio between 4–8 keV and 1–2 keV band is  $0.94 \pm 0.06$  and  $0.83 \pm 0.21$  in the range 1700–1900 pixels (off-WR) and 2000–2200 pixels (on-WR), respectively. This is consistent with the insignificant detection of nonthermal emission in the spectral analysis. In addition, we note that there are no X-ray decrement in any energy band at the WR, indicating that the nonthermal pressure of the WR is much weaker than that of thermal pressure.

## 4. Discussion

Suzaku has observed Abell 3376 twice and constrained the non-thermal hard X-ray emission. An upper limit on the excess emission above the thermal component obtained from the HXD PIN spectrum from a 34′×34′ (FWHM) region is  $<1.4 \times 10^{-11} \text{ erg s}^{-1} \text{ cm}^{-2}$  and  $<2.1 \times 10^{-11} \text{ erg s}^{-1} \text{ cm}^{-2}$  (15–50 keV) for the center/ER and the WR, respectively. These are similar to the BeppoSAX upper limit (Nevalainen et al. 2004). The XIS hard band spectrum of a 122 arcmin<sup>2</sup> region around the WR also gives a tight upper limit of  $<1.1 \times 10^{-12} \text{ erg s}^{-1} \text{ cm}^{-2}$  (4–8 keV). Thanks to the narrower field of view of the XIS and PIN compared to the BeppoSAX/PDS, some constraints on the energy density of the magnetic field and relativistic

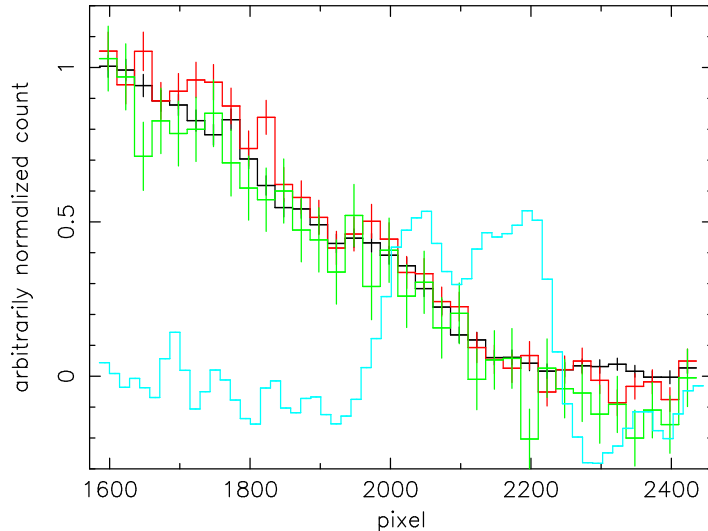


**Fig. 5.** X-ray count rate profiles in the 1–2 (black), 2–4 (red), and 4–8 (green) keV bands along the east-west direction, extracted from the white square region in figure 3. The 1.4 GHz radio profile is also plotted (light blue). Two point sources are located at pixels 1750 and 1970.

electrons can be obtained for a more limited region around the radio West Relic.

Assuming that the non-thermal emission originates from inverse Compton scattering of the CMB photons by relativistic electrons with energy of  $\gamma \sim 10^{4-5}$ , where  $\gamma$  is the Lorentz factor, we can estimate a lower limit on the magnetic field by combining the X-ray results here with the radio results. The 1.4 GHz integrated flux density of the Abell 3376 WR is  $82 \pm 5$  mJy (Bagchi 2002). Then the radio synchrotron luminosity becomes  $L_{\text{sync}} = 1.9 \times 10^{40}$  erg s $^{-1}$ , when integrated over a frequency range of 1–5 GHz, assuming a photon index of  $\Gamma = 2.0$ . The energy density of the CMB is  $U_{\text{CMB}} = 4.2 \times 10^{-13}(1+z)^4 = 5.0 \times 10^{-13}$  erg cm $^{-3}$ . Meanwhile, the upper limits of the IC X-ray emission are  $L_{\text{HXR}} < 2.4 \times 10^{44}$  erg s $^{-1}$  for the HXD (15–50 keV), and  $L_{\text{HXR}} < 2.2 \times 10^{43}$  erg s $^{-1}$  for the XIS (2–10 keV), under the assumption that the photon index is 2. These are shown in figure 6, together with the GLAST sensitivity limit. Using the relation  $L_{\text{HXR}}/L_{\text{sync}} = U_{\text{CMB}}/U_{\text{B}}$  (where  $U_{\text{B}} = \frac{1}{8\pi}B^2$ ), the magnetic field is estimated to be  $B > 0.03$   $\mu\text{G}$  for the HXD and  $B > 0.10$   $\mu\text{G}$  for the XIS, which do not rule out the equipartition condition of  $B \sim 0.5\text{--}3$   $\mu\text{G}$  (Bagchi et al. 2006). The XIS gave a significant constraint on non-thermal X-ray emission at the WR and yields an upper limit on the energy density of relativistic electrons in the WR of  $9.0 \times 10^{-13}$  erg cm $^{-3}$  or  $2.9 \times 10^{-13}$  erg cm $^{-3}$ , assuming the electron energy index of 3 or 2, respectively, and the minimum electron energy of  $\gamma \sim 10^2$ , below which the Coulomb losses are very fast. The thermal pressure around the WR is estimated from the temperature (3.8 keV) obtained by the XIS in this region and the thermal electron density ( $\sim 1 \times 10^{-4}$  cm $^{-3}$ ) obtained with ASCA/GIS (Fukazawa et al. 2004), giving  $\sim 1 \times 10^{-12}$  erg cm $^{-3}$ . Since there is no apparent X-ray decrement at the WR, the non-thermal pressure is likely smaller than the thermal pressure. In this case, the steep energy index of relativistic electrons around 3 is not

preferred if the minimum electron energy extends to  $\gamma = 10^2$ . The upper limit from the HXD gives an independent measurement of the total amount of relativistic electrons not necessarily emitting at 1.4 GHz radio band, but possibly at longer wavelengths. In the same way as the XIS case, the non-thermal pressure by the relativistic electrons averaged over a cube of 2.7 Mpc on a side (34' at the distance of A3376) is less than  $4.6 \times 10^{-13}$  erg cm $^{-3}$  or  $6.2 \times 10^{-14}$  erg cm $^{-3}$ , assuming tan electron energy index of 3 or 2, respectively. These are much smaller than the thermal pressure. This constraint is also valuable information if the magnetic field is strong only in the WR but the relativistic electrons are widely distribute around the WR.

Other mechanisms of non-thermal X-ray emission that we can consider are non-thermal bremsstrahlung and synchrotron. Since the former is very inefficient and will cause a large heat input into the ICM rather than emitting hard X-rays (e.g. Petrosian 2001), we think it will not be the dominant process for producing non-thermal hard X-rays in this particular cluster. X-rays from the synchrotron process need very high energy electrons with  $\gamma \sim 10^8$ . Since their life time is very short, around  $10^5$  year, primary electrons accelerated in situ are not realistic. Secondary electrons decaying from primary protons are possible candidates. The current upper limit on the X-ray to radio flux ratio allows an electron energy index of  $<2$ . In this case, GeV gamma-rays from decays of  $\pi^0$ s produced through protons and intracluster hot gas is expected and GLAST can detect such emission (Blasi 2002), without violating the HXD result.

In the next decade, hard X-ray observations with much higher sensitivity above 10 keV will become available from implementing new technologies such as the hard X-ray imager planned for the NeXT mission. Therefore, detection of hard X-ray emission is promising unless the emission is very extended.

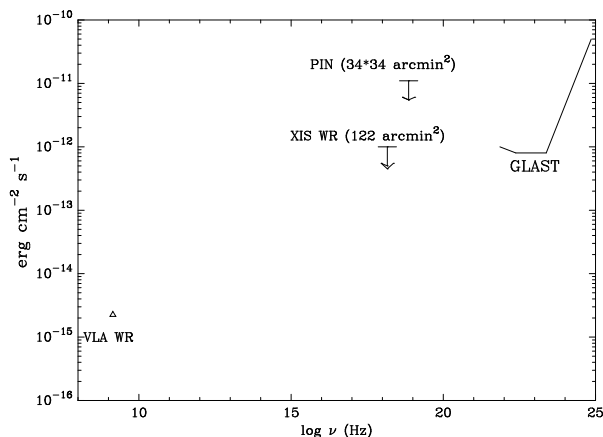


**Fig. 6.** Plot of the radio synchrotron and X-ray upper flux of A3376 WR non-thermal emission on the Spectral Energy Distribution. The sensitivity limit of GLAST is also shown.

## 5. Conclusion

Suzaku has observed Abell 3376 to search for non-thermal emission in clusters of galaxies. Thanks to the low background of the HXD PIN, a tight upper limit on the possible non-thermal flux is obtained for the Abell 3376 WR region. The XIS produced an upper limit on the non-thermal flux in the soft energy band (4–8 keV) for the first time. Although future improvements in the NXB reproducibility will yield increased sensitivity, our result already demonstrates the potential of the XIS and HXD/PIN to search for non-thermal emission from galaxy clusters.

Authors thank to Dr. J. Nevalainen for careful reading and many useful comments. NK is supported by Japan Society for the Promotion of Science Postdoctoral Fellowship for Young Scientists. JPH acknowledges support from NASA grant NNG06GC04G.

## References

- Blasi, P. 2002, astro-ph/0207361
- Bagchi, J. 2002, astro-ph/0210553
- Bagchi, J., Durret, F., Lima Neto, G. B., Paul, S., & Chavan, S. 2005, Proceedings of the 29th International Cosmic Ray Conference.
- Bagchi, J., Durret, F., Lima Neto, G. B., & Paul, S., 2006, *Science*, 314, 791
- Boldt, E. 1987, *IAUS*, 124, 611
- Condon, J. J. 1974, *ApJ*, 188, 279
- Fujita, Y., & Sarazin, C. L. 2001, *ApJ*, 563, 660
- Fukazawa, Y., Nakazawa, K., Isobe, N., Makishima, K., Matsushita, K., Ohashi, T., & Kamae, T. 2001, *ApJ*, 546, 87
- Fukazawa, Y., Makishima, K., & Ohashi, T., 2004, *PASJ*, 56, 965
- Fusco-Femiano, R., dal Fiume, D., Feretti, L., Giovannini, G., Grandi, P., Matt, G., Molendi, S., & Santangelo, A. 1999, *ApJ*, 513, 21
- Fusco-Femiano, R. et al. 2000, *ApJ*, 534, 7
- Fusco-Femiano, R., Dal Fiume, D., Orlandini, M., Brunetti, G., Feretti, L., & Giovannini, G. 2001, *ApJ*, 552, 97
- Giovannini, G., Feretti, L., Venturi, T., Kim, K. T., & Kronberg, P. P., 1993, *ApJ*, 406, 399
- Inoue, S., Aharonian, F., Coppi, P., & Sugiyama, N. 2006, poster presentation in “The Extreme Universe in the Suzaku Era”
- Ishisaki, Y. et al. 2007, *PASJ*, 59, 113
- Kaastra, J. S., Lieu, R., Mittaz, J. P. D., Bleeker, J. A. M., Mewe, R., Colafrancesco, S., & Lockman, F. J. 1999, *ApJ*, 519, 119
- Kawano, N. 2006, Ph-D. Thesis, Hiroshima University
- Kirsch, M. G. 2005, *Proc. SPIE* 5898, 22
- Kokubun, M. et al. 2007, *PASJ*, 59, S53
- Koyama, K. et al. 2007, *PASJ*, 59, S23

- Kushino, M., Ishisaki, Y., Morita, U., Yamasaki, N. Y., Ishida, M., Ohashi, T., & Ueda, Y. 2002, PASJ, 54, 327
- Mitsuda, K. et al. 2007, PASJ, 59, S1
- Mizuno, T. et al. 2006, *Suzaku-Memo* 2006-42
- Nakazawa, K., Makishima, K., & Fukazawa, Y. 2007, PASJ, 59, 167
- Nevalainen, J., Oosterbroek, T., Bonamente, M., & Colafrancesco, S. 2004, ApJ, 608, 166
- Petrosian, V. 2001, ApJ, 557, 560
- Serlemitsos, P. et al. 2007, PASJ, 59, S9
- Takahashi, T. et al. 2007, PASJ, 59, S35
- Takizawa, M., & Naito, T. 2000, ApJ, 535, 586
- Tawa, N. et al. 2007, PASJ, in press

## Appendix 1. PIN NXB Estimation

We give a full description of the PIN NXB estimation used in this paper in Kawano (2006). Here we briefly summarize it.

### A.1.1. Estimation Method

The NXB of the PIN detector depends strongly on the COR and the activation after the SAA passage (Kokubun et al. 2007). COR is the shielding power against charged particles in units of  $\text{GeV c}^{-1}$ , and the best parameter to predict the PIN NXB with good accuracy. Since the COR changes as the satellite's position above the earth changes, we first create PIN NXB maps using the earth occultation data from September 2, 2005 to March 11, 2006. The total exposure time is  $\sim 2$  Msec. The data are divided into 16 maps in eight energy band (0–11, 11–15, 15–20, 20–25, 25–32.5, 32.5–45, 45–70, 70–90 keV) and two kinds of orbital path (with or without SAA passage). Each map is binned by  $3 \times 3$  degree<sup>2</sup> so that one pixel typically contains 100–200 counts. Examples of maps for SAA or non-SAA passage orbits in the 15–20 keV band are shown in figure 7. The clear difference of NXB pattern due to activation in the SAA can be seen. When the time and position (i.e. latitude and longitude) are input, we can estimate the PIN NXB from these maps. Figure 8 left (red circles) shows the fractional residuals between the estimated PIN NXB and the observational data on sources sufficiently faint to be undetectable with the PIN. The signal in these observations can be regarded as CXB plus NXB. It is obvious that the residuals increase by  $\sim 10$  % as time goes by. This implies that it is necessary to take into account the long-term variation of PIN NXB.

Based on the above, we then go back to the NXB (e.g. earth occultation data) light curve and fit it with an empirical model including four time-variable component as follows,

$$\begin{aligned}
 BGD(t) = & A \times PINUD^2 + B \times PINUD \\
 & + C \times \left( \int PINUD \exp(-t_{SAA}/\tau) dt \right)^D \\
 & + E \times (1 + \sin(2\pi \times 2.3 \times 10^{-7} \times (t - F)))
 \end{aligned}$$

$$\begin{aligned}
& + G \times (1 - H \times \exp(-t/I)) \\
& + J \text{ (constant)}.
\end{aligned}
\tag{A1}$$

Here, capitals from A to J stand for the fitted variables. The first two terms give the COR dependence, which is well traced by the PINUD count. PINUD is a charged particle monitor included with the HXD. The terms with parameters C to I express the activation component. The short-term component is estimated by the PINUD build-up count; convolution of the PINUD count by an exponential function with an appropriate time constant (12500 sec). The middle-term component is found to produce an approximately periodic variation with  $\sim 50$  days, as a result of the modulation of SAA activation due to the precession of the Suzaku orbit, and thus it is represented by the sine curve. The term with G, H, and I represents the long-term component. We measure the free parameters A to J from fitting the light curve over the entire PIN energy range of 11-90 keV. We fit separately for those orbits with/without SAA passage. The light curve without SAA passage is shown in figure 8 right. The  $\chi^2$  root-mean-square (RMS) residuals with (without) SAA passage are  $1774/1009 = 1.76$  ( $1878/1413 = 1.33$ ), and  $\sim 6.8$  ( $6.3$ ) %, respectively. The contribution of each component for the total NXB counts is (a)  $\sim 73$  % for the COR-dependent terms, (b)  $\sim 22$  % for short-term, (c)  $\sim 5$  % for middle-term, and (d)  $< 1$  % for long-term activations, respectively. We correct the template PIN NXB maps by the effects of only components (c) and (d), since components (a) and (d) are already incorporated into the map data bases. After this procedure the long-term trend of the residuals in figure 8 left is reduced by this procedure. We generate an 8 energy-band NXB model spectrum for any observation using the corrected PIN NXB map and the actual satellite trajectory of the observation on the map.

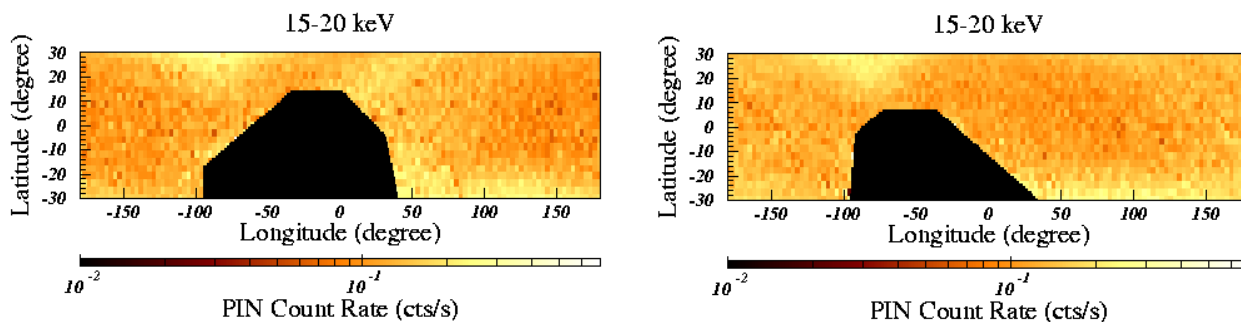


**Fig. 7.** Examples of PIN NXB maps. Left and right are in the 15–20 keV band, with and without SAA passage, respectively. One pixel is  $3 \times 3$  degree<sup>2</sup>. Filled black area in each map corresponds to the SAA region.

In order to confirm the reproducibility of the estimated PIN NXB, we compared the count rates predicted by the NXB model with real dark earth data for 100 observations each of whose exposure is longer than 3000 sec (i.e. more than  $\sim 1000$  cts). We furthermore chose



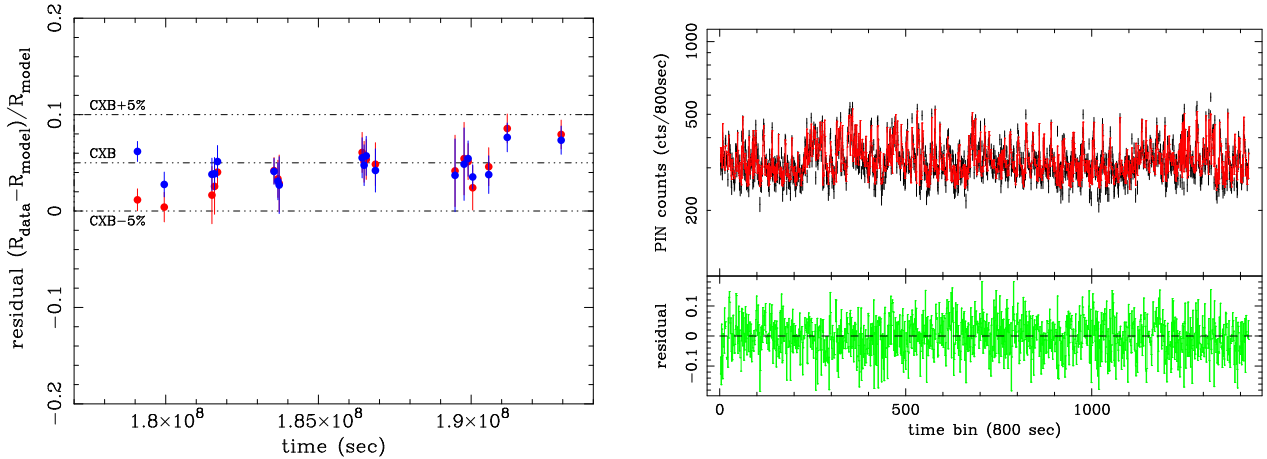


**Fig. 8.** The left figure shows the time dependence of the fractional residual between the dark earth data and the NXB model. Red points are for the NXB estimation from the raw map data, and blue points are after the long-term variation of the NXB is corrected. Three dot-dashed lines represent the level of 0.95, 1.00, and 1.05 of the CXB, which is itself only 0.05 of the NXB. The right top figure shows the light curve of the PIN NXB data (black) fitted with the empirical model (red) over 6 months. See the text for details. The right bottom panel shows the fractional residual between the NXB data and the model of the PIN NXB (green). Horizontal axis represents the order of time-sorted data bins.

an exposure of  $> 30000$  sec since data of shorter exposure suffer a large statistical error. As shown in Figure 9, the model and data are in good agreement within  $\sim 5\%$ . We made the distribution histogram of  $\sum_i \frac{\sqrt{(d_i^2 - m_i^2) - e_i^2}}{m_i}$ , where  $d_i$ ,  $m_i$ ,  $e_i$  are the real NXB count rate, model NXB rate, and real NXB statistical error. We fitted the histogram with a Gaussian whose Gaussian parameter  $\sigma$  is 2%. In other words, a systematic error in our NXB estimation is  $\sim 2\%$  at  $1\sigma$ .

#### A.1.2. Check of the Estimated PIN NXB for the Abell 3376 Center/ER Observations

We here check the estimated PIN NXB in two different ways. Apart from our PIN NXB model, there are two other models (bgd\_a, bgd\_d) developed and supplied by the HXD team. The first (bgd\_a) mainly uses the PINUD rate and the PINUD build-up with a fixed decaying time constant. The second (bgd\_d) estimates the NXB with an empirical time-variation model, which is obtained by fitting the light curve of the earth occultation data with a more complex model than that in the previous subsection. As described in §3.1, the NXB estimation of the above two models is not accurate for the observation of the WR region. On the other hand, they are available for the observation of the center/ER region. Therefore, we can check the consistency between three model NXBs. Figure 10 left shows the comparison of the background-subtracted spectra. They are almost consistent within statistical errors. The spectrum using bgd\_a gives a somewhat low count rate. Such a tendency is seen in the report of background reproducibility (Mizuno et al. 2006) in the early phase of Suzaku observations.

The constancy of the NXB-subtracted light curve is also useful to check the background

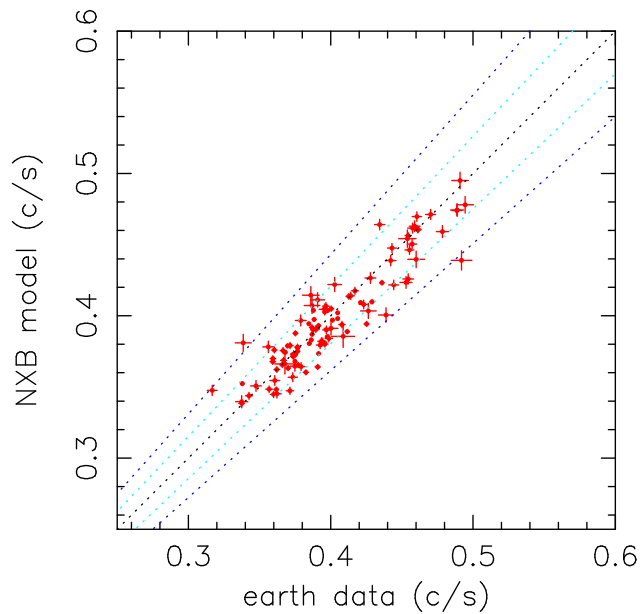


**Fig. 9.** Comparison of count rate between the estimated NXB and the real dark earth data for 100 observations. Dotted lines represent 5 % (light blue) and 10 % (blue) deviation level.

reproducibility for stable source such as galaxy clusters. The 3000 sec binned light curve of the Abell 3376 Center/ER observation in 15–70 keV is shown in figure 10 right. It is found that the light curve is constant with time within statistical errors. The same results are also obtained for the WR pointing and other observations. We also investigated the NXB-subtracted spectra obtained in three different periods in each observation of A3376, and confirmed consistency among the three spectra within statistical errors.

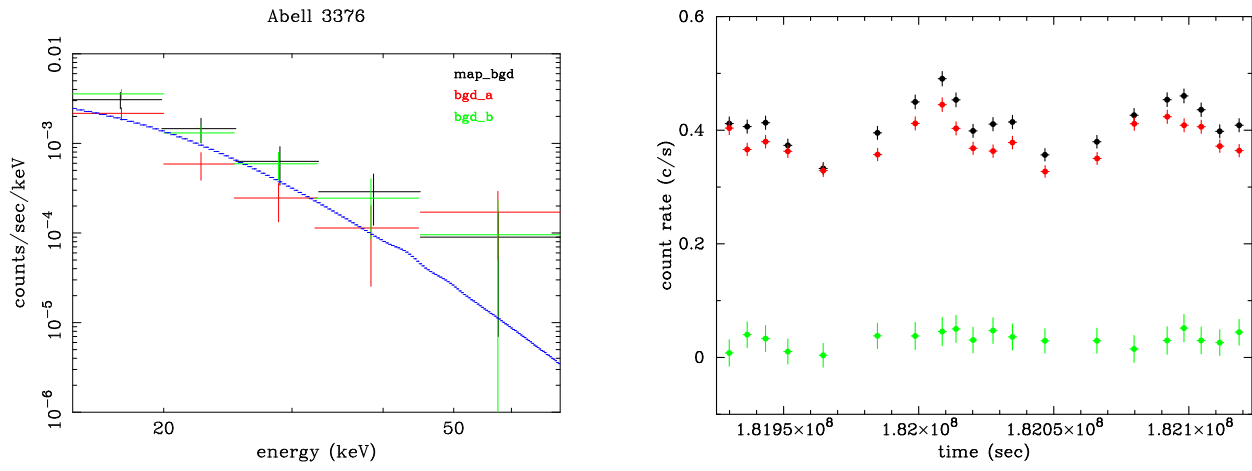


**Fig. 10.** Comparison of background-subtracted spectra (left) and light curve (right) of the A3376 center/ER region (Oct. 6–10, 2005). Black points in the left panel are the spectra from which the NXB estimated by our method is subtracted. Red and green points use the officially supplied NXB models of `bgd_a` and `bgd_d`, respectively. the CXB level is given by the blue line. In the right panel black, red, and green data points are the total count rate, the NXB model with our method, and the background-subtracted count rate, respectively.